



# Assessment of aerial thermography as a method of in situ measurement of radiant heat transfer in urban public spaces

Marta Videras Rodríguez<sup>a</sup>, Sergio Gómez Melgar<sup>b,\*</sup>, José Manuel Andújar Márquez<sup>b</sup>

<sup>a</sup> Programa de Doctorado de Ciencia y Tecnología Industrial y Ambiental, Centro de Investigación en Tecnología, Energía y Sostenibilidad – CITES (Research Centre for Technology, Energy and Sustainability), Universidad de Huelva, Campus La Rábida, Palos de la Frontera (Huelva) 21810, Spain

<sup>b</sup> TEP192 Control y Robótica, Centro de Investigación en Tecnología, Energía y Sostenibilidad – CITES (Research Centre for Technology, Energy and Sustainability), Universidad de Huelva, Campus La Rábida, 21810, Palos de la Frontera (Huelva), Spain

## ARTICLE INFO

### Keywords:

Unmanned aerial vehicle (UAV)  
Thermography  
Mean Radiant Temperature (TMRT)  
Urban thermal comfort  
Urban sustainability

## ABSTRACT

Urban public spaces are an essential part of the urban environment, supporting social relationships and promoting a healthy lifestyle among citizens. However, the high value of urban land has led to an over-urbanisation of cities, increasing urban heat stress and decreasing the number and size of public spaces. Rising air temperatures in cities – known as the urban heat island effect (UHI) - combined with global warming, make public spaces less comfortable. For these reasons, there has been a growing concern to improve the thermal comfort of urban spaces. Thermal radiation is a determining factor in urban thermal comfort and is normally summarised in a value called mean radiant temperature ( $T_{MRT}$ ). In the past, conventional methods have been used to calculate it, such as net radiometers and globe thermometers. In recent years, the scientific community has used ground-based handheld thermal cameras for its quantification. However, there is a lack of literature on the use of aerial thermography for this purpose (i.e. an unmanned aerial vehicle (UAV) equipped with a thermal infrared device). Given this gap in the literature and the advantages in time, versatility and accuracy of these systems, this paper presents a new method for assessing the measurement of radiant heat transfer in a pedestrian urban space using aerial thermography. From the surface temperatures of the infrared imagery collected by the UAV,  $T_{MRT}$  was estimated at multiple points in a pedestrian area of a subtropical city (Huelva, Spain) during a typical summer day. In order to verify accuracy of the proposed method to estimate the  $T_{MRT}$ , a microclimate urban simulation was carried out using ENVI-met v5. The comparative analysis of the measured and simulated dataset verified the applicability of aerial thermography for the measurement of radiant heat transfer (with  $R^2$  values of 0.98 for the data set and 0.8 for the data of each time period). To conclude, new strategies were proposed to improve urban thermal comfort and to make cities more sustainable.

## 1. Introduction

Outdoor public space is the setting for everyday social interaction where activities take place in order to satisfy collective urban needs. Outdoor spaces promote an active lifestyle through social, cultural and leisure activities, improving people's physiological and psychological health (Niu et al., 2015). However, the increasing urbanisation of cities has generated a level of heat stress, that combined with the impact of global warming, encourages users to stay longer indoors where comfort conditions are satisfied by artificial air conditioning. This trend contributes to a sedentary lifestyle that is harmful to human health and significantly increases building energy consumption (Kumar and

Sharma, 2020; Rodríguez et al., 2020). In recent years, the scientific community has contributed to the development of new methodologies both to achieve energy efficiency in buildings and thermal comfort conditions in urban spaces (Lai et al., 2019; Johansson et al., 2014; Gómez Melgar et al., 2020; Melgar et al., 2018). The comfort conditions of a public space are decisive, as they determine the use and permanence of users. Increasing thermal comfort could therefore increase the time people spend outdoors.

Human thermal comfort is defined as the “state of mind in which human feels satisfied within the thermal environment” according to ASHRAE (“The American Society of Heating, Refrigerating & Air-Conditioning Engineers”) (RA-C, 2001). The scientific community has

\* Corresponding author.

E-mail addresses: [marta.videras245@alu.uhu.es](mailto:marta.videras245@alu.uhu.es) (M.V. Rodríguez), [sergomel@uhu.es](mailto:sergomel@uhu.es) (S.G. Melgar), [andujar@uhu.es](mailto:andujar@uhu.es) (J.M.A. Márquez).

<https://doi.org/10.1016/j.scs.2022.104228>

Received 16 April 2022; Received in revised form 26 August 2022; Accepted 29 September 2022

Available online 1 October 2022

2210-6707/© 2022 The Authors. Published by Elsevier Ltd. This is an open access article under the CC BY-NC-ND license (<http://creativecommons.org/licenses/by-nc-nd/4.0/>).

evaluated thermal comfort in public spaces in two ways: “transversal field survey” and “longitudinal subject test”. The first method is based on the vote of the users who evaluate the thermal comfort of the public space and give information about their gender, age, clothing and mood at the time of the interview. The collection of votes is followed by the monitoring of the surrounding microclimate, the activities taking place and the time involved (Canan et al., 2019). The second method also analyses environmental thermal parameters and is based on the recording of physiological parameters of the subjects such as skin temperature, heart rate, pulse and sweating (Lai et al., 2020).

Thermal comfort is quantified by environmental index which usually combines two or more parameters into a single variable. Environmental index simplify the description of the thermal environment and the stress imposed by an environment (A.-C., 2001). The best-known index are PMV (predicted mean value), SET (standard effective temperature) and PET (physiological equivalent temperature) (Kumar and Sharma, 2020). PMV index gives the average thermal sensation of a collective of persons utilizing the psychophysical ASHRAE-scale. PMV is related to the imbalance between the actual heat flow from the body in a given environment and the heat flow required for optimum comfort at the specified activity (Fanger, 1972). To calculate it, it is necessary to determine the human metabolic rate, the thermal balance of the human body and four environmental variables (air temperature, mean radiant temperature, relative humidity and wind velocity) (Jendritzky and Nübler, 1981; Golasi et al., 2018). SET index is defined as the equivalent temperature of an isothermal environment (environment at sea level, in which air temperature is equal to the mean radiant temperature and wind velocity is zero) at 50 % relative humidity in which a subject, while wearing clothing standardised for the activity concerned, would have the same heat stress and thermoregulatory strain as in the actual test environment (Xi et al., 2007). It depends on micrometeorological parameters and on the thermal load of the skin, so skin temperature, skin moisture and skin saturated water steam are crucial. The PET index is defined as the air temperature required to reproduce in a standardised environment and for a standardised person the core and skin temperatures observed in the conditions being evaluated (Höppe, 1999). It is relative to thermal clothing insulation, metabolic rate, skin temperature, core temperature, mean radiant temperature, air temperature, wind velocity and water steam pressure (Golasi et al., 2018).

Thermal comfort depends on multiple factors that can be classified as direct and indirect. Direct factors are physical (thermal radiation, air temperature, wind and humidity), physiological (skin temperature, sweat rate, thermal insulation/moisture permeability of clothing) and psychological (expectation, experience, autonomy). Indirect factors are behavioural (attendance, changing clothes), site (microclimatic factors), personal (gender, age), and cultural (ideal of beauty, sun preference, cultural norms), among others (Fig. 1).

The thermal radiation is defined by the energy balance; in other words, by the continuous transfer of heat by conduction and convection between the elements found in the urban space: mainly pavements, façades, vegetation, water and pedestrians (Zhao et al., 2020). The surface

temperature of the materials found in the urban space is directly associated with the Urban Heat Island (UHI) effect (Naughton and McDonald, 2019). Some thermal properties of materials such as the evaporation and solar radiation absorption capacity (during the day) and the storage capacity (during the night) influence the heat stress perceived by users in urban areas. Changes in surface properties caused by urban development, such as the replacement of urban green areas by artificial materials with high absorption of solar radiation, lead to an increase in land surface temperature (LST) and result in this phenomenon (Song and Park, 2020). Thus, the temperatures of urban areas become higher than those of suburban areas.

The temperatures of individual surfaces are usually combined into a mean radiant temperature ( $T_{MRT}$ ). The  $T_{MRT}$  is a key variable that simplifies radiant heat transfer in making thermal calculations for the human body (Guo et al., 2020). The most commonly used methods of in situ assessment of  $T_{MRT}$  are based on the use of globe thermometers, net radiometers or thermography. The globe thermometer is a hollow sphere, painted black, with a thermometer bulb inside. From the globe temperature, the emissivity and the diameter of the sphere, the globe's mean convection coefficient, the air temperature and the wind velocity, it estimates the value of  $T_{MRT}$  (Bedford and Warner, 1934; Chen et al., 2014). Net radiometers are used to calculate  $T_{MRT}$  by integral radiation measurements with view factors. It is a more complex device with a moving axis composed of 12 sensors formed by pyrgeometers, to measure long-wave radiation, and pyranometers, to measure short-wave radiation (VDI 1994; Thorsson et al., 2007). The method using an IR camera estimates  $T_{MRT}$  from temperatures of the surfaces that enclose the point. According to the Stefan-Boltzmann's law surface temperatures are converted into radiation, and then weighted with view factors to calculate  $T_{MRT}$  (Zhao et al., 2020; Lee et al., 2019). Computer simulation is also commonly used for estimation of the  $T_{MRT}$ , as it allows for simplification of the calculations. Software such as ENVI-met, RayMan, SOLWEIG etc. are used for assessment by means of simulation (Salata et al., 2016; Matzarakis et al., 2007; Lindberg et al., 2008).

The scientific community has focused on evaluating and comparing each of the above methodologies. In previous research, it was evaluated  $T_{MRT}$  in a large open square in Sweden using three of the methodologies: the globe thermometer, the net radiometer and RayMan software. They concluded that the differences between the first two methods were small, underestimating the short-wave radiation using the globe thermometer. The simulation method showed best results at midday on a typical summer day, at high sun elevations (Thorsson et al., 2007). Recently, it was compared the correlations and discrepancies between the  $T_{MRT}$  values derived from a globe thermometer, a net radiometer and three simulation models (ENVI-met, RayMan and SOLWEIG) in a university campus in a typical severely cold city from China. In this case, the globe thermometer and ENVI-met proved to be the most suitable methods to estimate  $T_{MRT}$  in summer (Du et al., 2021).

Developments in infrared thermography have provided new opportunities in recent years to estimate  $T_{MRT}$ . The use of handheld thermal cameras for this purpose has been validated and compared to conventional methods like the globe thermometer and the net radiometer (Zhao et al., 2020; Cohen et al., 2020; Acuña Paz y Miño et al., 2020). The scientific community proposed a new software called Mr.T to evaluate the mean radiant temperature in urban canyons using thermography and solar data collected from the nearest weather station data. However, this software tool can only be applied in public spaces with an urban canyon morphology (Cohen et al., 2020). Recently, it was presented a new method that combines thermal images captured from the ground with a handheld thermal camera using imagery software with a three-dimensional model, previously generated by a drone equipped with an RGB camera (Zhao et al., 2020). The complexity of creating hybrid models can be saved by equipping both cameras in the aircraft saving time of inspection and during the post-processing phase, as both tasks can be automated. However, there is a lack of literature on the use of thermal infrared technology equipped in unmanned aerial

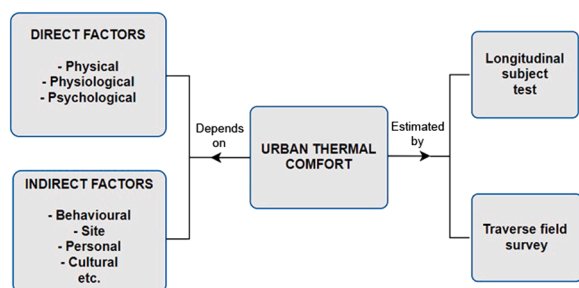


Fig. 1. Factors influencing urban thermal comfort and estimation methods diagram.

vehicles (UAVs) to investigate urban thermal comfort, especially at micro-scale (Videras Rodríguez et al., 2021).

Aerial thermography has many advantages for measuring the surface temperature of an urban space. In terms of time, aerial thermography allows to register the surface temperatures of all pavements and façades in a single flight saving researchers' time during on-site measurement. The possibility of planning flight routes for the drone to fly automatically, regulating its speed and autonomy, optimises the time and also the economy of these missions by reducing the number of operators required. Although the initial investment in an UAV may be more expensive than other methods, it is necessary to highlight the versatility of these aerial systems, which can incorporate many sensors and be useful for multiple tasks. Collecting data from several sensors increases the possibilities of working with them. Many different types of data can be collected in a single inspection, depending on the sensors installed on the UAV. Regarding the accuracy of the aerial thermography, the scientific community has assessed the variability of urban ground surface temperatures using drone observations and they have demonstrated several advantages compared to satellite or in situ imagery (Naughton and McDonald, 2019; Song and Park, 2020; Gaitani et al., 2017; Feng et al., 2020). Compared to the use of handheld thermal cameras, aerial thermography enables the acquisition of more thermal information because it can capture a larger dimension of terrain if the flight height is increased from a nadir perspective. Recent advances in this technology have enabled the development of thermal cameras with high thermal resolution to avoid a loss of sensitivity as the distance to the target increases. Respect to satellite imagery, the spatial resolution of UAV-images allows for more accurate and small-scale temperature data collection in the urban environment. In addition, while satellite imagery is limited to daily or weekly observations, UAV-images can capture temperature changes throughout the day at any time. This advantage allows to have a quick observation of spatial and temporal evolutions in scenarios of changing architecture and to obtain images that can be overlapped in time. This is an advantage for analysing the dynamics of occupation of different public spaces. Some research has been carried out using UAVs equipped with RGB cameras to monitor the activity of public parks assessing other indirect factors of urban thermal comfort such as the number of people, activities, duration, change of clothes, gender, age, etc (Park et al., 2020).

Based on the literature reviewed (Table 1), no previous works have been found dealing with the use of aerial infrared pictures for estimating  $T_{MRT}$ . Given this gap in the literature and the advantages in time, versatility and accuracy of these systems, this paper presents a new method for assessing the measurement of radiant heat transfer in a pedestrian urban space using an UAV equipped with a thermal infrared device. The paper is structured as follows: the materials and the definition of the method are presented in section 2. This section specifies: (i) the spatial configuration of the study area - a square in the historic centre of a subtropical city in southern Spain (Huelva); (ii) the method of data acquisition at three different times during a typical summer day at 11:00 h, 15:00 h and 19:00 h based on two types of survey (aerial and in situ surveys); (iii) the post-processing phase of thermal images to extract the temperature data; (iv) the  $T_{MRT}$  calculation method; and (v) the urban microclimatic simulation performed with the ENVI-met tool. The results are shown in section 3. First, the surface temperature variations of materials in the urban area are evaluated. Then, the  $T_{MRT}$  is calculated at 20 fictitious points in the pedestrian space and the spatial distribution of thermal radiation is estimated. Subsequently, comparative analysis of the measured and simulated data set verifies the applicability of aerial thermography for this purpose. Section 4 discusses the results and section 5 draws the main conclusions of the research and proposes new strategies to improve thermal comfort of the pedestrian space.

2. Materials and methods

Table 1  
Summary of literature review.

Area	Topic	Author	Refs.
Research on human thermal comfort and environmental index	Review of thermal comfort studies in urban open spaces	P. Kumar and A. Sharma	(Kumar and Sharma, 2020)
	Standardised information on indoor and outdoor thermal comfort	The American Society of Heating, Refrigerating and Air-Conditioning Engineers (ASHRAE)	(A.-C., 2001)
	A transversal field survey to quantify outdoor thermal comfort	F. Canan et al.	(Canan et al., 2019)
	Review of thermal comfort studies in urban open spaces	D. Lai et al.	(Lai et al., 2020)
	Thermal comfort analysis and applications: equations for its quantification and environmental index	P. O. Fanger	(Fanger, 1972)
	Quantitative model for the assessment of thermal urban climate (Environmental Index: Predicted mean vote, PMV)	G. Jendritzky and W. Nübler	(Jendritzky and Nübler, 1981)
	Outdoor thermal comfort standardisation (Environmental Index: Global outdoor comfort index, GOCl)	I. Golasi et al.	(Golasi et al., 2018)
	Study on outdoor thermal comfort in subtropical climate (Environmental Index: Standard effective temperature, SET)	T. Xi et al.	(Xi et al., 2007)
	Universal environmental index for the outdoor thermal assessment (Physiological equivalent temperature, PET)	P. Höppe	(Höppe, 1999)
	Studies of $T_{MRT}$ by conventional methods	Review of quantitative assessment of $T_{MRT}$ in indoor and outdoor environments	H. Guo et al.
Estimation of radiant heat by means of the globe thermometer		T. Bedford and C. G. Warner	(Bedford and Warner, 1934)
Comparison of $T_{MRT}$ outdoor calculation between different methods: net radiometer, globe thermometer and simulation models		Y. C. Chen et al.	(Chen et al., 2014)
Standardised information on the impact of solar radiation on outdoor thermal comfort		Verein Deutscher Ingenieure (VDI Guideline)	(VDI 1994)
		S. Thorsson et al.	

(continued on next page)

Table 1 (continued)

Area	Topic	Author	Refs.
	Comparison of $T_{MRT}$ outdoor calculation between different methods: net radiometer, globe thermometer and simulation models		(Thorsson et al., 2007)
	Indoor $T_{MRT}$ estimation in a large stadium using manual IR imagery	D. S. Lee et al.	(Lee et al., 2019)
	Outdoor $T_{MRT}$ estimation in urban canyons using ground-based handheld IR imagery and net radiometer	S. Cohen et al.	(Cohen et al., 2020)
	Outdoor $T_{MRT}$ estimation using ground-based handheld IR imagery combined with photographic techniques	J. Acuña Paz y Miño et al.	(Acuña Paz y Miño et al., 2020)
Studies of $T_{MRT}$ by simulation tools	Evaluation of outdoor thermal comfort using ENVI-met simulation	F. Salata et al.	(Salata et al., 2016)
	Evaluation of outdoor thermal comfort using RayMan simulation	A. Matzarakis et al.	(Matzarakis et al., 2007)
	Evaluation of outdoor thermal comfort using SOLWEIG simulation	F. Lindberg et al.	(Lindberg et al., 2008)
	Comparison of $T_{MRT}$ outdoor calculation between different simulation tools: ENVI-met, RayMan and SOLWEIG	J. Du et al.	(Du et al., 2021)
Research on IR combined with UAVs technology for urban thermal comfort	Urban $T_{MRT}$ analysis using a hybrid model between UAV RGB imagery and ground-based handheld IR imagery	X.Zhao et al.	(Zhao et al., 2020)
	Comparison between urban land surfaces temperature using drone observations	J. Naughton and W. McDonald	(Naughton and McDonald, 2019)
	Using aerial and ground-based thermal data to measure the temperature of various land cover materials	B. Song and K. Park	(Song and Park, 2020)
	Review of the use of UAVs equipped with IR technology in urban applications	M. Videras et al.	(Videras Rodríguez et al., 2021)
	Analysis of thermal characteristics of materials and land surface temperature distribution using UAV-equipped multispectral imaging sensors	N. Gaitani et al.	(Gaitani et al., 2017)
	Comparison between urban land surfaces temperature using drone observations	L. Feng et al.	(Feng et al., 2020)
		K. Park et al.	

Table 1 (continued)

Area	Topic	Author	Refs.
	Monitoring the activity and comfort status of public parks users using UAV RGB imagery		(Park et al., 2020)

### 3. Materials

In this section the materials used to carry out the experimentation are detailed. For in situ data acquisition (2.3.1), it was used a Testo 875 1i handheld thermal camera (Testo<sup>TM</sup>, Titisee-Neustadt, Germany) and a thermo-hygrometer RS-91 Pro (RS Components<sup>TM</sup>, Corby, United Kingdom). The handheld thermal camera was used with a diffuse reflector and PVC electrical insulating tape to calculate the emissivity of the materials at the study site. On the other hand, the thermo-hygrometer was used to measure air temperature and outdoor relative humidity. For aerial data acquisition (2.3.2), it was used a DJI Mavic 2 Enterprise Advanced (DJI<sup>TM</sup>, Nanshan, Shenzhen, China) equipped with a RGB and a thermographic camera. It was attached a parachute for safety reasons in urban public space.

Two thermal cameras were used in this study, a manual one for emissivity calculation and an aerial one equipped on the UAV for material analysis and  $T_{MRT}$  calculation. The manual thermal camera has a limited thermographic resolution (160×120 px) compared to the thermographic resolution of the IR sensor equipped on the drone (640×512 px). The higher the resolution of the sensor, the higher the accuracy of the measurements, the larger the objects that can be captured and the greater the distance at which measurements can be taken. Since the calculation of the emissivity can be performed in situ by making various adjustments on the camera (without the need for a post-processing phase) and only requires an image close to the material (with a diffuse reflector and a PVC tape attached to it, as described in section 2.3.1 In situ measurement), the handheld thermal camera was used to perform this task.

Several software tools were used: in relation to the UAV, it was used DJI Pilot for planning mission in aerial data acquisition (2.3.2), and DJI Thermal Analysis tool and DJI Terra for post-processing of the images (2.4) captured by the UAV. ENVI-met (ENVI-met<sup>TM</sup>, Essen, Germany) was used for the urban microclimatic simulation (2.6). Details of the materials mentioned are given in Table 2.

### 4. Study area






This study was conducted in an urban pedestrian area in the historic city centre of Huelva, located in the southwest of Spain (6°56'24''O, 37°15'58''N). Huelva is in the CSA climatic zone according to Köppen-Geiger climate classification (Peel et al., 2007). Its climate is typical Subtropical-Mediterranean with Atlantic influences. In general, it has mild, windy and partly cloudy winters (with temperatures rarely falling below 5 °C), and hot, dry and clear summers (the warmest months are July and August when temperatures can occasionally exceed 40 °C). The annual average temperature is 18.2 °C, the annual average humidity is 66 %, and the annual average rainfall is 525 mm (Annual climatological values 2022).

UAV survey and in-situ measurements were performed in summer, on 20 July 2021. The study area chosen was a pedestrian square with high foot traffic located in front of one of the most important churches in the city, San Pedro Church (Fig. 2).

San Pedro Square has an area of 1125 m<sup>2</sup> (45 m x 25 m) and is located around four cobblestone roads between 4 – 7 m wide (the area of the urban space analysed taking into account the road is 2115 m<sup>2</sup>). To the north are several 2-storey residential buildings, to the east 4-storey, to the south 3-storey and to the west is the 25 m high church. The



**Table 2**  
Material specifications.

Material	Model	Specifications
 Thermal camera	Testo 875 1i	Spectral band: 8-14 $\mu\text{m}$ Thermal sensitivity < 50 mK IR Resolution: 160x120 pixels Lens: HQ 32° x 23° with manual focus, automatic hot/cold spot detection Measuring range: -30 °C ~ 350 °C
 Thermohygrometer	RS-91 Pro	Humidity range: 0.0 ~ 100.0 % Temperature range: 20.0°C ~ 60.0°C Humidity Measurement Resolution: 0.1 % Temperature Measurement Resolution: 0.1°C
 UAV	DJI Mavic 2 Enterprise Advanced	Takeoff Weight (without accessories): 909 g Dimensions: 322x242x84 mm (unfolded) Max speed: 72 km/h Max flight time: 31 min Spectral band: 8-14 $\mu\text{m}$ Thermal sensor resolution: 640x512 pixels Measuring range: -40 °C ~ 550 °C Digital zoom: 32x digital zoom, 16x thermal zoom
 DJI Software	DJI Pilot DJI Terra DJI Thermal Analysis Tool	
 Simulation Software	ENVI-met	v5 LITE version

building façades are covered with coloured plastic paint (72,8%), brick tiles (16.9%) and ceramic blocks (10.5%). As specified in Fig. 3, the square is covered with granite tiles and pebble stone mosaics. The boundaries are surrounded by four dirt paths with 10 palm trees between 3 and 15 m high (covering an approximate area of 300 m<sup>2</sup>, less than 15% of the total analysed area) and a terrazzo tiled pavement next to the road. In summary, the urban space of St. Peter’s Square used for the circulation of people accounts for 53.2% compared to the space dedicated to the circulation of vehicles around it, which is 46.8% paved with cobblestone road. The paving of the square is 17.2% covered with pebble stone mosaics, 16.5% covered with granite tiles, 12% covered



**Fig. 2.** San Pedro Square. 3D Model of RGB imagery from UAV.

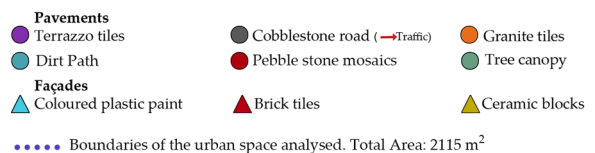


**Fig. 3.** Orthophoto of RGB imagery from UAV with color-coded points by ground/façade cover type.

with dirt path and 7.5% with terrazzo. Fig. 4 shows the actual view of the types of paving and cladding of the façades.

### 5. Data acquisition

The survey was carried out at three different times (11:00 h, 15:00 h, 19:00 h) on 20 July 2021. Since the objective was to analyse the variation of the mean radiant temperature during a typical summer day, three time periods with solar exposure were chosen, corresponding to the morning (11:00 h), midday (15:00 h) and evening (19:00 h). It was divided into two parts, an in situ and an aerial inspection, which were carried out at the same time by a team of two people.

During the in situ inspection the pavement and façade materials were identified and their emissivity was calculated. Then, air temperature and relative humidity were measured at 32 points around the square (Fig. 5). These points were chosen for two reasons: 20 points inside the square for the analysis of the mean radiant temperature and the paving (granite tiles and pebble stone mosaics), and 12 points outside the square for the analysis of the rest of the paving (terrazzo tiles, cobblestone road and dirt path). The 20 points of analysis of the mean radiant temperature



Fig. 4. Actual images of pavements and façades materials.

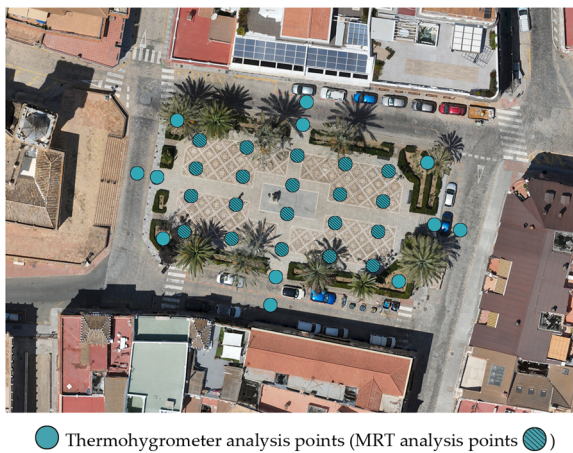


Fig. 5. Orthophoto of RGB imagery from UAV with thermohygrometer in situ measurement.

inside the square were distributed in 4 rows following the horizontal axis of the square and 5 columns following the vertical axis of the square. In this way, any pedestrian walking through the entrances of the square would be analysed.

The aerial survey was carried out with an UAV equipped with a thermal and RGB camera that captured a total of 1862 images (930 thermal images and 930 RGB images). Subsequently, the RGB and IR images were processed to obtain orthophotos and 3D models, and also, from the thermal images, the surface temperature data needed to calculate the  $T_{MRT}$  were extracted. Finally, to verify the results obtained, a microclimatic simulation was performed with ENVI-met software. Fig. 6 shows a diagram of the methodology used.

### 5.1. In situ measurement

Before inspection, using the Testo 875 1i handheld thermal camera (Table 1), thermal images were taken of the materials shown in Fig. 4. A diffuse reflector, i.e. a material with high reflectivity (such as aluminium foil), was placed near each material, from which the apparent reflected temperature was extracted, assuming an emissivity of 1 in the thermal camera. Then, PVC electrical insulating tape (of known emissivity: 0.95) was attached, its surface temperature was captured, compared to the surface temperature of the material, and both values were adjusted to obtain the actual emissivity value of the material. The emissivity values obtained ranged from 0.90 (for the cobblestone road) to 0.96 (for the

dirt path). 0.93 was set as the average emissivity of the urban scene and 20 °C was set as the average apparent reflected temperature. Both values were used in 2.3 section: post-processing of UAV IR images.

During in situ inspection, the thermohygrometer RS-91 Pro was used (Table 2) to record air temperature and relative humidity at different points distributed along the square, as shown in Fig. 5. The average air temperature recorded was 25.7 °C at 11:00 h, 30.7 °C at 15:00 h, 28 °C at 19:00 h in San Pedro Square. The average relative humidity recorded was 56.2 % at 11:00 h, 48.6 % at 15:00 h and 55 % at 19:00 h. In addition, to calculate the mean long-wave radiant temperature, these mean air temperature and relative humidity values were also used in the post-processing step of the thermal images. These data were recorded by one operator at the same time as the aerial surveys were being carried out by another operator.

Once the survey was completed, hourly climatic data were extracted for wind (wind direction and velocity) and solar radiation (global ( $S_t$ ), diffuse ( $S_d$ ) and direct ( $S_b$ ) irradiance on a horizontal surface, and altitude ( $\gamma$ ) and zenith ( $\psi$ ) solar angles) for the three time periods measured on 20 July, from the nearest weather station located on the outskirts of the city (5 km from the historic centre) in order to complete the calculation of the mean short-wave radiant temperature and the input of climate data in the simulation tool (VDI 2022; VDI 2022; VDI 2022).

### 5.2. Aerial measurement

Planning an UAV flight mission in an urban and densely populated area is a complex task with associated risks. In Spain are mandatory by law, the previous acquisition of permissions from AESA (Agencia Estatal de Seguridad Aérea, State Aviation Safety Agency), the Spanish Ministry of the Interior and the City Council of the city where it is going to fly. For these actions, the registration of the operator, the pilot and the UAV are mandatory. In addition, the regulations require the drone to weigh less than 10 kg and to be equipped with an airbag or parachute system to reduce the kinetic energy of impact (< 80 J) in the event of an accident. In urban scenario, the flight must be within the visual range of the pilot and below 120 m, a horizontal safety distance from buildings must be respected and the study area must be cordoned off to prevent the transit of people below the UAV's flight (VDI 2022).

Before aerial inspection, a visual survey mission was carried out to determine the flight height, according to the observed building heights, in order to plan a safe collision-free flight mission. The mission planning was carried out by the DJI Pilot software, which allows the drawing, based on a satellite image, of the waypoints that the aircraft will follow during the flight. In each time period, 2 flights were planned, an automatic flight at +80 m and a manual flight at +3 m, which were carried



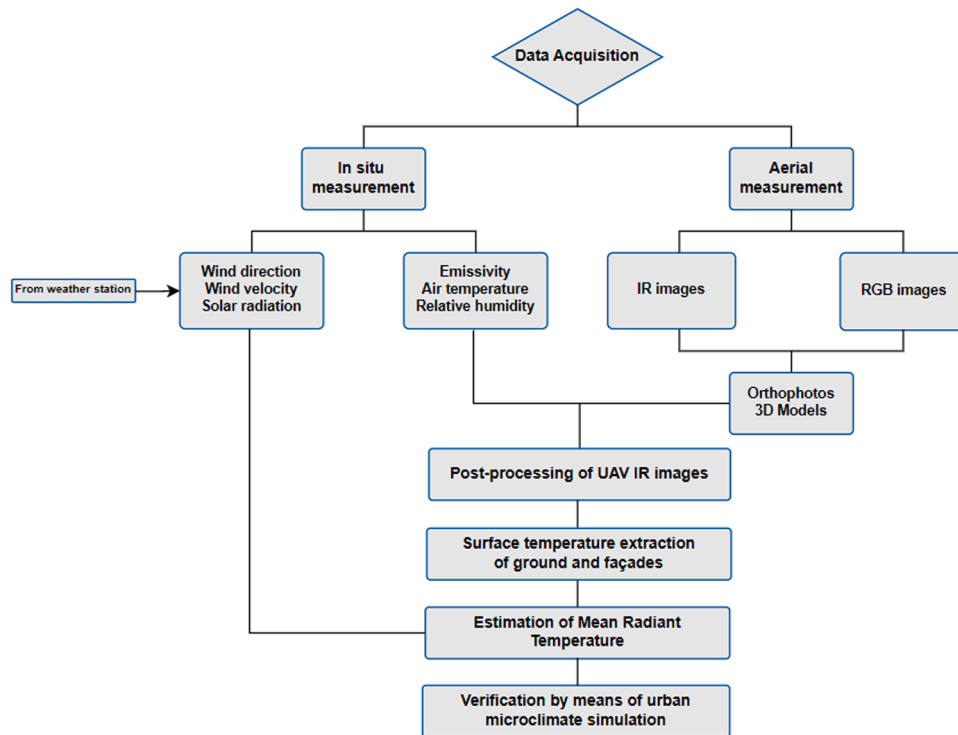


Fig. 6. Methodology diagram.

out in 40 minutes, requiring approximately two batteries. First, the automatic flight was structured in 5 phases: one phase of nadir flight (90 °) and four phases of oblique flight at 60 °, in order to generate, in the post-processing phase, an orthophoto and a three-dimensional model of the square and its surroundings. Afterwards, the manual flight was carried out at an angle of 0 ° capturing images of the four façades that border the square.

During the inspection, the weather conditions were ideal in the early morning, a day with light cloud cover and little wind which progressively increased during the day (1.8 m/s at 11:00 h, 4.5 m/s at 15:00 h and 6.6 m/s at 19:00 h). The DJI Mavic 2 Enterprise Advanced (M2EA) was chosen to carry out the inspection due to its low weight and the high performance of its thermal camera (Table 1). The M2EA is a lightweight, easily transportable, foldable multicopter with articulated arms and a take off weight of 909 g. It can reach a maximum speed of 72 km/h. It is equipped with an RGB camera to capture HD images and 4K video, and a radiometric thermal camera to measure pixel temperature of thermal images. Its high-resolution camera sensors support a 32x digital zoom and a 16x thermal zoom. Both cameras work at the same time capturing visual, thermal or view-split images. Its 640×512 px thermal resolution results in clear images and the ability to take a closer look at fine detail from a greater distance. The drone was equipped with a light 40 g parachute as shown in Fig. 7.

6. Post-processing of UAV IR images

Once all the thermal images captured by M2EA were collected, they were post-processed in the DJI Thermal Analysis Tool software. To perform quantitative thermography, i.e. to obtain real temperature data from a thermal image, post-processing is necessary to compensate for the emissivity, reflected apparent temperature and atmosphere of each image. The emissivity compensation is necessary to correct the apparent temperature displayed by the camera as the emissivity indicates how much infrared radiation is emitted by the surface of the object. If the emissivity is high, the apparent temperature will be close to the actual body temperature, if it is low, the apparent temperature will be closer to



Fig. 7. Aerial measurement device – DJI Mavic 2 Enterprise Advanced.

the actual temperature of the surrounding objects. The compensation of the reflected apparent temperature is necessary to compensate the infrared radiation from the environment that is reflected on the surface of the object to be measured. Finally, the compensation of the atmosphere, which disturbs the radiation between the camera and the object, is achieved through the entry of the values of air temperature, relative humidity and distance to the object at the time of the image capture.

Once the emissivity, reflected apparent temperature and atmosphere of each set of images per time slot were compensated, the temperature field (or thermal focus) was also manually adjusted per set of images to get an uniform temperature range. From this point, the temperature

values of the materials and analysis points were extracted using the measurement tools provided by the software. The surface temperature of the facades was extracted at a height of 1.5 m, the standardised height at which  $T_{MRT}$  is assessed in urban public spaces. Then, in order to generate orthophotos and three-dimensional models (in both spectral ranges), the DJI Terra software was used. This software transforms images and allows to create and edit point clouds, high-precision 2D maps and 3D models. These processes are performed automatically because of its CPU core based on photogrammetry techniques and artificial vision algorithms. By means of a grid interpolation of the dense point cloud obtained by the sensors, a three-dimensional model of the public space was obtained. All the individual images were combined into RGB and thermal orthomosaic images to obtain various orthophotos of the entire area of interest. There are other photogrammetry software on the market to perform this type of task such as Pix4DMapper and Agisoft Metashape, but their use is not compatible with the files extension captured by the M2EA.

## 7. Estimation of mean radiant temperature ( $T_{MRT}$ )

In the outdoor environment, the radiation energy transfer (heat loss or gain by thermal radiation) is the most important heat flux for the human heat balance, mainly in sunny conditions (Kántor and Unger, 2011). According to ASHRAE, the  $T_{MRT}$  is the uniform temperature of a fictitious black-body radiation enclosure (with emission coefficient  $\varepsilon = 1$ ) that results in the same net radiation energy exchange with the occupant as the actual environment, a more complex radiation environment (Arens et al., 2016). It is defined as the radiant temperature from long-wave radiation from interior surfaces expressed as a spatial average of the temperature of surfaces surrounding the occupant, weighted by their view factors with respect to the occupant. Most recently in 2017, ASHRAE added more complexity by expanding their definition for  $T_{MRT}$  to include both the short-wave and long-wave components:  $t_{fsw}$  or short-wave  $T_{MRT}$  that accounts for direct and diffuse solar radiation, and  $t_{rlw}$  or long-wave  $T_{MRT}$  that characterizes the radiation from interior surfaces weighted by their view factors. The  $T_{MRT}$  is a parameter that synthesises the effects of the complex radiant environment (long-wave and short-wave radiation) in one temperature-dimension index (Guo et al., 2020).

The solar or short-wave radiation is composed of the radiation intensity of the sun on a surface perpendicular to the incident radiation direction ( $I$ ) and the diffuse solar radiation and the diffusely reflected global radiation ( $D$ ). The terrestrial or long-wave radiation is composed of atmospheric and environmental thermal radiation ( $E$ ) (Matzarakis et al., 2007; Kántor and Unger, 2011). To calculate  $T_{MRT}$ , the surroundings of the human body are divided into  $n$  isothermal surfaces ( $i=1$  to  $n$ ) with the surface temperature  $T_i$ , the emissivity  $\varepsilon_i$  and the weight factor  $F_i$ . Both long-wave radiation ( $E$ ) and diffuse-reflected short-wave radiation ( $D$ ), are emitted from each of the  $n$  surfaces of the surroundings. This result in a value for  $T_{MRT}$  compiled by Fanger (1972) and Jendritzky et al. (1981) (Fanger, 1972, Jendritzky and Nübler, 1981):

$$T_{MRT} = 4 \sqrt{\frac{1}{\sigma} \sum_{i=1}^n \left( E_i + ak \frac{D_i}{\varepsilon_p} \right) F_i} \quad (1)$$

Where  $\sigma$  is the Stephan-Boltzman constant ( $5.67 \cdot 10^{-8} \text{ W}/(\text{m}^2\text{K}^4)$ ). Short-wave solar radiation ( $D$ ) and long-wave radiation ( $E$ ) are weighted by weight factors ( $F$ ). In this study, weight factors were assigned following the six-direction radiation method that assumes human body like a uniform cylinder proposed by Höppe (1992) (Höppe, 1992). This model, normally used for biometeorological applications, defines weighting factors for an urban space in which measurements of radiative flux density are made for long-wave and short-wave in six directions ( $i$ ): upward, downward and horizontal flux from the four orthogonal directions. Following the Eq. (1), the radiation absorbed by the human body is weighted by two absorption coefficients:  $ak$  for short-wave

radiation and  $al$  for long-wave radiation, which depend on skin and clothing. These are generally assumed to be 0.7 for short-wave radiation and 0.97 for long-wave radiation, being the latter equivalent to the emissivity coefficient of human skin ( $\varepsilon_p$ ).

$T_{MRT}$  is incremented to  $T_{MRT}^*$ , if there is also direct solar radiation ( $I$ ):

$$T_{MRT}^* = 4 \sqrt{\frac{1}{\sigma} \sum_{i=1}^n \left( E_i + ak \frac{D_i}{\varepsilon_p} \right) F_i + \frac{fpakI}{\varepsilon_p\sigma}} \quad (2)$$

Where  $I$  is weighted with the surface projection factor ( $f_p$ ) that is a function of the incident radiation direction ( $\gamma$ , solar altitude angle) and the body posture, proposed by VDI standards (1998, 2001) (The association of German engineers) (VDI 1998; VDI 2001). The value of  $I$ , the direct irradiance on a surface perpendicular to the beam depends on the direct irradiance on a horizontal surface ( $S_b$ ) and the solar zenith angle ( $\psi$ ), as determined G.S Campbell et al. (Campbell and Norman, 1998).

$$S_b = I \cos\psi \quad (3)$$

On the one hand, using aerial thermography, radiant flux densities of long-wave radiation ( $E_i$ ) were computed from the Stefan-Boltzman equation for surrounding walls, the ground and the sky (Cohen et al., 2020):

$$E_i = \varepsilon_i \sigma (273,15 + T_i)^4 \quad (4)$$

Where  $T_i$  is the temperature of surface  $i$  and  $\varepsilon_i$  is the emissivity of surface  $i$ . For the sky, surface temperature was supposed equal to air temperature and its emissivity was computed using the water steam pressure in air (which is influenced by the air temperature and relative humidity) (Campbell and Norman, 1998).

On the other hand, the diffuse-reflected short-wave radiation ( $D$ ) is composed by the diffuse solar radiation from the sky ( $S_d$ ) and the reflected global radiation from the ground and the surfaces ( $S_r$ ) (Kántor and Unger, 2011). The reflected radiation is the product of the average surface reflectance for the solar waveband  $p_s$  (albedo) and the global irradiance on a horizontal surface  $S_t$  (that compiles direct plus diffuse) (Campbell and Norman, 1998). An hourly value of the reflected radiation was obtained and assumed constant for the ground and the surrounding walls.

$$S_r = p_s S_t \quad (5)$$

The value of  $p_s$  was set at 0.15, a standard value for urban areas (Campbell and Norman, 1998).

## 8. Microclimate urban simulation. Verification of $T_{MRT}$

In order to verify accuracy of the proposed method to estimate the  $T_{MRT}$ , a microclimate urban simulation was carried out using ENVI-met v5. This software is useful for creating microclimatic models based on the fundamental laws of fluid dynamics and thermodynamics and simulates the interactions between the surface, plants and the atmosphere in urban environments. It allows creating three-dimensional models and calculating temperature, humidity, wind flows, turbulence, radiation fluxes, mean radiant temperature etc. with a high spatial resolution (between 0.5 and 5 m horizontally) and temporal resolution (up to 5 s).

ENVI-met is probably the world's leading software for the analysis of the effects of climatology, architecture and urban planning on cities (Tsoka et al., 2018). This software has previously been used in combination with aerial thermography to calibrate simulated models comparing urban surface temperatures (Fabbri and Costanzo, 2020). For calculating  $T_{MRT}$ , it has also been widely used and validated by comparing the results with both other simulation tools and conventional methods (Du et al., 2021; Naboni et al., 2017; Gál and Kántor, 2020; Claudia Carfan, 2020).

In this research, the free version of ENVI-met (LITE version) was used - which has limitations in domain size and types of analysis. Two main



input files are required for the simulations: the area input file, which defines the project location parameters and the design of the urban space, building types, vegetation and soil; and the configuration file, which contains the simulation settings related to the meteorological parameters. The study area was input as a domain of  $40 \times 30 \times 10$  cells of  $2 \times 2 \times 2$  m size each and the location was fixed in Huelva (Spain). For buildings, the façade material was set by default (with moderate insulation) and the roofing material was tile. Different pavements materials were chosen according to the different materials found in the study area: basalt bricks for roads, loamy soil for dirt paths, and concrete and granite pavements for walkable areas. As for the vegetation, trees were assimilated to the palm tree typology with plant height of 15 m and 5 m. These adopted values for the urban materials are the default ones provided by ENVI-met libraries. Measured data in situ related to air temperature and relative humidity were used for the meteorological boundary condition with Simple Forcing. The climate data extracted from the weather station were used for the boundary conditions for wind and solar radiation. The output setting and output interval for files were 60 min in three time sets (11:00 h, 15:00 h and 19:00 h).

Once the simulations were performed,  $T_{MRT}$  values were obtained at the same analysis points and the data were compared with the values calculated using two statistical metrics: coefficient of determination ( $R^2$ ) and root mean square error (RMSE) (Willmott, 1981).  $R^2$  describes the proportion of the total variance explained by the model, in other words, it is a measure of the goodness-of-fit or reliability of the estimated model to the data. RMSE is the standard deviation of the residuals (prediction

errors). Residuals are a measure of the distance of the data points from the regression line. RMSE indicated the total model error.

## 9. Results

According to the methodology previously described, the results obtained in the research are shown below. In the first section, the surface temperatures of the study area extracted from the infrared images are analysed. In the second section, the  $T_{MRT}$  was calculated in 20 fictitious points distributed in the urban area. Finally, in the third section, the results of the  $T_{MRT}$  are validated by simulation using ENVI-met software.

### 9.1. Ground and façade surface temperature variation

Fig. 8 shows the RGB and TIR orthophotos captured by the UAV throughout a typical summer day. Two profile lines with North-South and West-East orientation were drawn to analyse in depth the ground surface temperatures and air temperature at the main accesses of the study site. The thermal field was adjusted per set of images to get an uniform temperature range, thus the maximum and minimum temperature values define the temperature scale displayed beside the images.

At a general view of the square and its closest surroundings, the maximum surface temperature recorded was  $59.0^\circ\text{C}$  at 15:00 h and the minimum surface temperature was  $16.0^\circ\text{C}$  at 11:00 h. The thermal field with the highest temperature values and the greatest thermal amplitude was at 15:00 h with a difference of  $35.0^\circ\text{C}$  between the maximum value

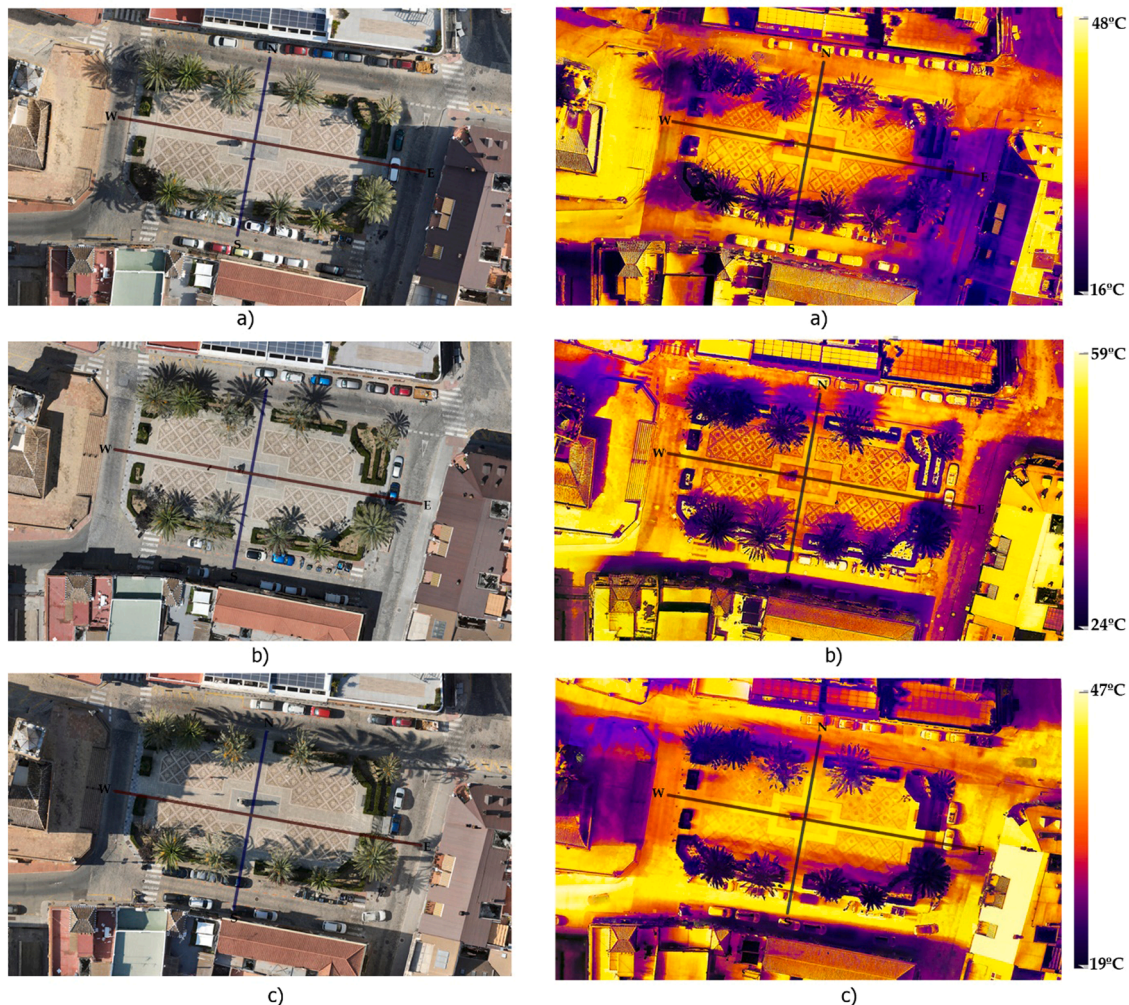


Fig. 8. Orthophotos of RGB and thermal imagery from UAV. A) At 11:00 h, B) At 15:00 h, C) At 19:00 h.

(59.0 °C) and the minimum value (24.0 °C). The 11:00 h and 19:00 h temperature scales showed similar maximum and minimum values, between 16.0 °C and 19.0 °C as minimum values, and between 48.0 °C and 47.0 °C as maximum values, respectively.

Using aerial RGB images, it was possible to analyse the variation of shadows as time progresses from a fixed and zenith viewpoint. Given the orientation of the square (aligned 10 ° with respect to North) and the solar altitude (maximum at this time of the year), at 11:00 h the main shadows were generated by buildings in the east access to the square and the east road. At 15:00 h, the shadows were produced by trees in the south front of the square and the north road. At 19:00 h, the west access to the square and the west road were shaded by the church.

In Figs. 9,10, the two temperature profile lines with North-South and West-East orientation were plotted at different times to compare thermal values according to urban materials and shadows. When the ground surface temperature profile was analysed for line N-S, the average surface temperature was 26.9 °C at 11:00 h, 40.9 °C at 15:00 h and 35.6 °C at 19:00 h, resulting a maximum difference of 14 °C. For line W-E, it was 26.4 °C at 11:00 h, 43.0 °C at 15:00 h and 36.9 °C at 19:00 h (maximum difference of 16.6 °C). The mean air temperature was similar in both profiles with an average of 25.7 °C at 11:00 h, 30.7 °C at 15:00 h and 28 °C at 19:00 h, obtaining a thermal amplitude of 5 °C.

At 11:00 h, the granite located in the centre of the square was the material that reached the highest surface temperature, at 31.3 °C in N-S profile and at 30.0 °C in W-E profile. Minimum surface temperatures were located at the eastern access at 18.1 °C on the terrazzo and cobblestone road (both shaded by the building), and at the southern access at 19.5 °C. At these points, the lowest air temperature of 24.5 °C was recorded.

At 15:00 h, in N-S profile, the highest and lowest temperatures were recorded on the cobblestone road of the southern access road. It was reported 48.2 °C in the sunny area and 31.2 °C in the shaded area by the southern building. At this point, another minimum peak surface temperature was also recorded, at 33.9 °C, apparently in a sunny area but which had previously been shaded by a parked car. The maximum air temperature was also registered at 33.2 °C at the southern access. The northern half of the profile recorded below average surface temperature measurements (32.5-37.8 °C). In W-E profile, the maximum surface temperature and maximum air temperature were both recorded in the western access at 50.8 °C and 32.5 °C, respectively. In contrast, the minimum surface temperature and minimum air temperature were measured at the east access (28.5 °C and 29 °C, respectively).

At 19:00 h, the profiles trend was similar to 15:00 h. The highest and lowest surface temperatures were recorded in the southern access (43.7 °C and 24 °C) due to the shade generated by the building. The maximum air temperature was also registered at 30 °C at the southern access. There

was also a greater record of sub-average surface temperature measurements, around 29.4-33.3 °C, in the northern half of the profile. However, the east access indicated higher surface and air temperatures (41.1 °C and 29.9 °C) than the west access (30.6 °C and 25.3 °C), shaded by the church.

Using the data measured throughout the day, the surface temperature variations of the materials under sunny conditions were compared (Fig. 11). The trend in the temperature variation of the materials was very similar: temperatures were cooler at 11:00 h, reached the maximum temperature at 15:00 h, and cooled down at 19:00 h.

When the surface temperature characteristics of each ground cover type were investigated through the profile analysis, it was found that the cover type with the maximum surface temperature was the cobblestone road in all measured time periods. The surface temperature of the cobblestone road remained the highest among all surfaces starting at 11:00 h in the morning (35.2 °C), followed by dirt path (34.5 °C) and granite (32.5 °C). At 15:00h, the maximum surface temperature registered was cobblestone road (55.8 °C), followed by dirt path and terrazzo that both reached 53.2°C. At 19:00h, the highest surface temperature measured was cobblestone road (46.2 °C), followed by terrazzo (44.9 °C), granite (41.0 °C) and pebble stones pavement (41.0 °C). The dirt path, which had registered above average temperatures at 11:00 h and 15:00 h, was the material that cooled faster during the afternoon (39.1 °C), registering 14 °C less at 19:00 h.

On the other hand, the cover types with the lowest surface temperature were the materials identified on façades, on vertical surfaces, with brick tiles being the warmest façade material (T°max: 39.2 °C at 15:00 h) and ceramic blocks (T°min: 22.6 °C at 11:00 h) the coldest. The tree canopy showed the lowest temperature record in all measured time periods (26.0 °C at 11:00 h, 29.9 °C at 15:00 h, and 28.0 °C at 19:00 h).

### 9.2. Spatial distribution of T<sub>MRT</sub>

Once the surface temperature of the materials was analysed, the T<sub>MRT</sub> was calculated at 20 fictitious points distributed along the area under study. Fig. 12 shows the location of the analysis points and Fig. 13 gives the T<sub>MRT</sub> value at these points. Four lines of points were analysed: A and D on the longitudinal sides of the square next to the vegetation (A in the north side, D in the south side), and B and C on the longitudinal sides of the centre of the square. Each line was subdivided into 5 points a, b, c, d and e (a being the point to the west and e the point to the east).

At 11:00 h, the T<sub>MRT</sub> values showed a similar trend in the four lines of analysis (b>c>d>a>e). The highest T<sub>MRT</sub> values for each line were found at point b (Ab, Bb, Cb, Db), being point Cb, located in a central position of the square, the one that recorded the highest T<sub>MRT</sub> (37.2 °C). The lowest T<sub>MRT</sub> values for each line were found at point e (Ae, Be, Ce,

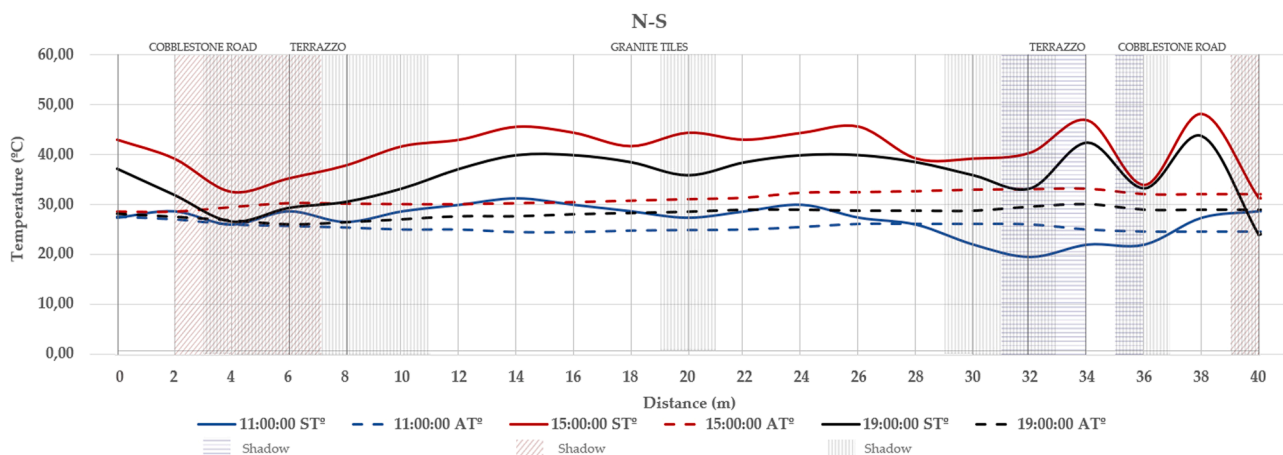


Fig. 9. Ground surface temperature. North-South profile.



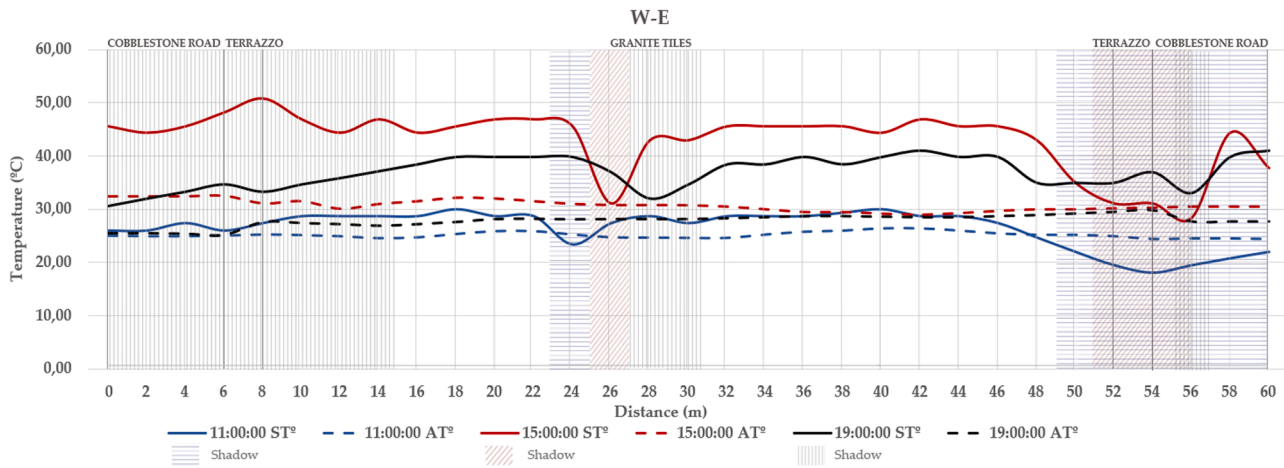


Fig. 10. Ground surface temperature. West-East profile.

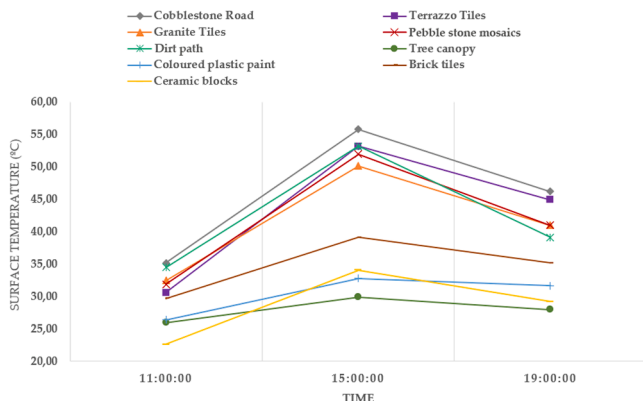


Fig. 11. Surface temperature materials in sunlight.



Fig. 12. Orthophoto of RGB imagery from UAV with  $T_{MRT}$  measurement points.

De), located at the eastern boundary of the square. The point that recorded the lowest  $T_{MRT}$  (34.6 °C) was point Ae. The difference in  $T_{MRT}$  between them was 2.6 °C.

The lowest  $T_{MRT}$  values were obtained in line A, adjacent to the northern vegetation, with a difference of 1 °C between the highest point (Ab: 35.6 °C) and the lowest (Ae: 34.6 °C). Lines B and D showed very close values with a difference of 0.1 °C between points. The line with the highest  $T_{MRT}$  values for each point was the central line C, with a maximum difference of 1.5 °C between the highest point (Cb: 37.2 °C) and the lowest (Ce: 35.7 °C). The thermal difference between line C and

line A was in the range of 1.1-1.6 °C. The thermal difference between line C and lines B-D was about 0.1-0.4 °C.

At 15:00 h, the four lines of analysis followed a same pattern:  $e > b > c > a > d$ . The highest  $T_{MRT}$  values for each line were at point e (Ae, Be, Ce, De). The point Ce, located in the east boundary of the square, was the highest  $T_{MRT}$  value (43.1 °C). The lowest  $T_{MRT}$  values for each line were at point d (Ad, Bd, Cd, Dd). The lowest value (40.4 °C) was recorded at point Dd. The thermal amplitude between the maximum and the minimum value was 2.7 °C.

Line D, bordering the south vegetation, showed the lowest  $T_{MRT}$  values, with a difference of 1 °C between the highest point (Ae: 41.4 °C) and the lowest (Ad: 40.4 °C). Line A, in the northern boundary, was very close to line D. Both lines showed close values of about 0.2-0.5 °C between points. The thermal difference between lines A-D and B was in the range of 0.7-1.4 °C. The line with the highest  $T_{MRT}$  values for each point was the central line C, with a maximum difference of 0.9 °C between the highest point (Ce: 43.1 °C) and the lowest (Cd: 42.2 °C). The thermal difference between line C and line B was about 0.5-0.8 °C.

At 19:00 h, the  $T_{MRT}$  values followed a same pattern:  $b > c > e > d > a$ , except for the northern boundary line D where  $a > d$ . The highest  $T_{MRT}$  value was 33.9 °C at points Bb and Cb, located in a central position of the square. The lowest  $T_{MRT}$  value was recorded at point Aa (31 °C), located at the north-western boundary of the square. The difference in  $T_{MRT}$  between them was 2.9 °C.

The lowest  $T_{MRT}$  values were obtained in boundary lines A and D, adjacent to the northern and southern vegetation respectively, with a difference of about 0-0.8 °C between points. The line A showed lower  $T_{MRT}$  values at points to the west (Aa: 31 °C, Ab: 32.5 °C, Ac: 32.3 °C) while the line D showed lower  $T_{MRT}$  values at Dd: 31.4 °C, in the centre east. The highest  $T_{MRT}$  values were obtained in the central lines B and C, with line C being 0.3 °C higher than line B. Line C recorded values between 32.6 °C (Ca) and 33.9 °C (Cb). The thermal difference between lines B-C and lines A-D was about 0.5-1.6 °C.

9.3. Verification of  $T_{MRT}$

Fig. 14 shows the linear relationship between  $T_{MRT}$  (simulated vs measured) considering the data collected in the 3 samples (11.00 h, 15:00 h, and 19:00 h). Results show a strong coefficient of determination ( $R^2$ ) between all points analysed (120 samples) throughout July 20 ( $R^2 = 0.987$ ) (Fig. 14d). The root mean square error (RMSE) was 0.43, which represents a 2.7 % with respect to the mean of the whole analysed data (36.7 °C).

Analysing the hourly datasets separately, results show a minor, but strong correlation at 11:00 h ( $R^2 = 0.80$ ) (Fig. 14a), at 19:00 h ( $R^2 = 0.78$ ) (Fig. 14c), with the best results obtained with the data collected at

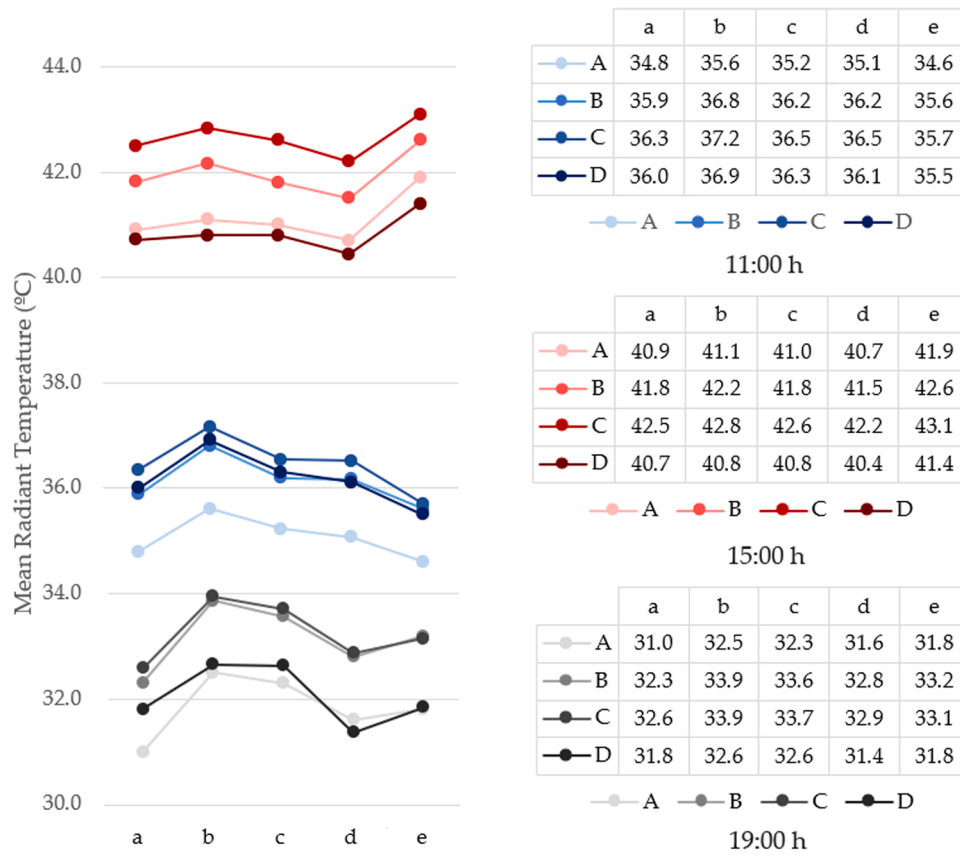


Fig. 13.  $T_{MRT}$  variation.

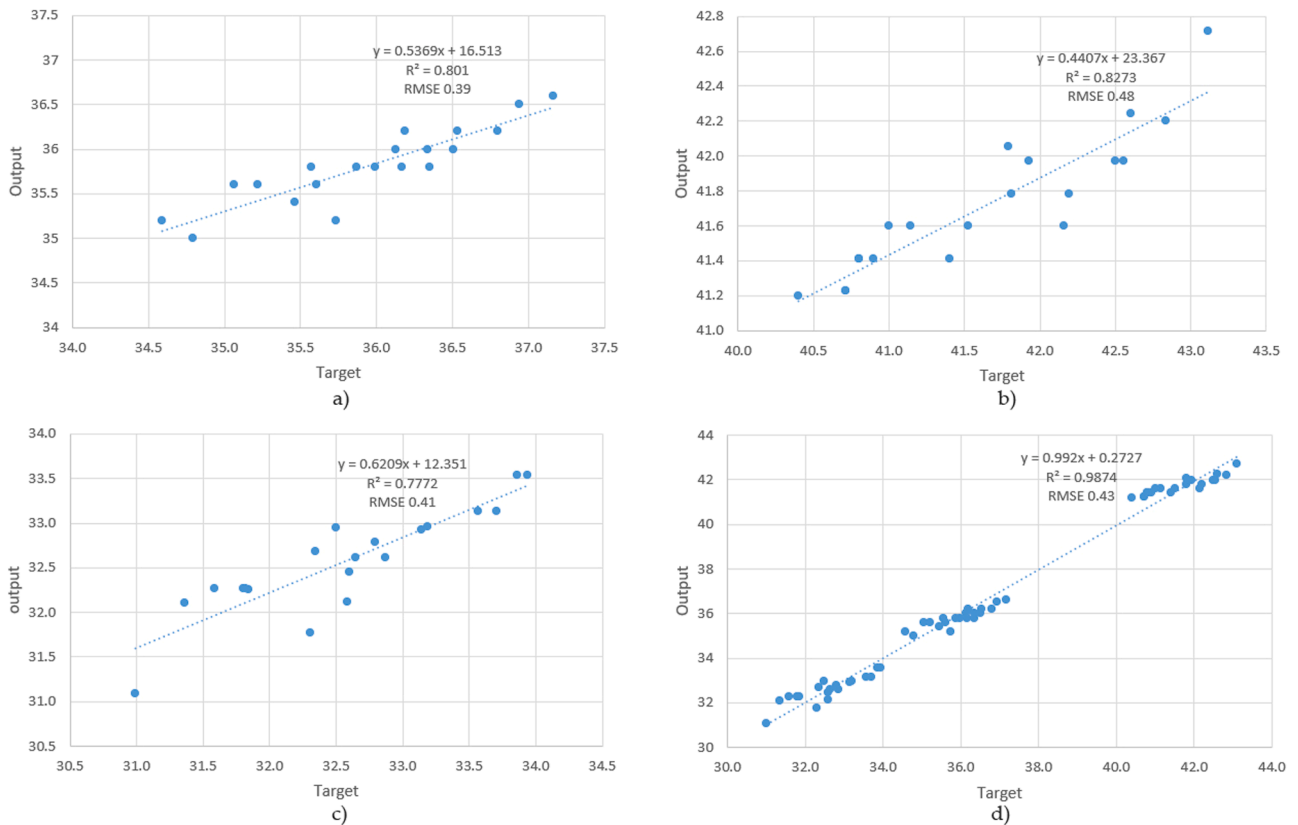


Fig. 14. Comparison of  $T_{MRT}$  simulated vs measured ( $R^2$  and RMSE): a) at 11:00 h, b) 15:00 h, c) 19:00 h and d) 20 July.



15:00 h ( $R^2 = 0.83$ ) (Fig. 14b). This is because although RMSE values of the estimation remain similar despite the hour of the sample (was 0.39 at 11:00 h, 0.48 at 15:00 h and 0.41 at 19:00 h), when considering a smaller fraction of the data, the coefficient of determination is more sensible. The RMSE represents a 2.8 % in relation to 35.9 °C at 11:00 h, 2.4 % in relation to 41.7 °C at 15:00 h and 3.1 % in relation to 32.6 °C.

## 10. Discussion

This study focuses on aerial thermography as a method of in situ measurement of thermal radiation values in urban public spaces. From a general perspective, through the review of the surface temperatures of materials in public space and the review of the methods used to measure  $T_{MRT}$  (IR and simulation software), it is shown that the IR method - equipped in UAV - is an advantageous option to apply to urban public spaces.

The use of RGB aerial imagery allowed to identify the variation of shadows over a typical summer day from a fixed and zenith viewpoint (Fig. 8). In combination with the thermal aerial images, the surface temperatures of two fictitious profiles with north-south and east-west orientations (Figs. 9,10) were analysed to evaluate the surface temperature (along with the air temperature) on the two main axes of the square (aligned with the four access points located at the cardinal points). Through these analyses, it was possible to evaluate in depth the cooling capacity of the shade on different pavements. The minimum surface temperature records were largely coincident with the shaded areas identified a priori in the RGB images. However, it is necessary to highlight the importance of thermal inertia in the influence of shadows comparing RGB images with thermal images. As observed in the results, the cooling effect of shadows is prolonged in time despite the surface is exposed to the sun again. It was also observed that, due to the prolonged exposure of the materials to the sun and their ability to store heat, while at 11:00 h the surface and air temperatures were similar (around 26 °C), at 19:00 h the surface temperature was 9 °C higher than the air temperature (28 °C). When comparing the surface and air temperatures in the two profiles, a greater variability in surface temperature was observed with respect to air temperature.

Analysing the surface temperature of the individual materials in Fig. 11, a similar trend was observed between them: the surface temperature was low in the morning, reached a maximum at midday and dropped again in the afternoon. The cover type with the highest surface temperature was the cobblestone road in all measured time periods (reaching 55.8 °C at 15:00 h). This may be due to the impact of vehicular traffic, as areas with high foot or vehicle traffic exhibit higher surface temperature variabilities than comparable surfaces with less traffic (Naughton and McDonald, 2019). On the other hand, the tree canopy recorded the lowest temperature (reaching 26.0 °C at 11:00 h) and remained very close to the air temperature throughout the day. In the three time periods studied, it was observed that the paving of the square, composed of granite tiles and pebble stone mosaic, recorded lower surface temperatures than the surrounding materials (cobblestone pavement, terrazzo and dirt path).

Once all the surface temperatures of the surroundings were extracted from the thermal images, the  $T_{MRT}$  value was calculated at 20 fictitious points distributed in the square along four lines: A, B, C, D (with W-E orientation) and five points: a, b, c, d, e (with N-S orientation) (Fig. 12). From the  $T_{MRT}$  spatial distribution (Fig. 13), it can be demonstrated that there is a wide variability in mean radiant temperatures behaviour across the urban public space due to material properties, vegetation influence and urban geometry, such as the orientation. Throughout a typical summer day, the trend in the four lines of analysis was similar, with the central lines B and C recording higher mean radiant temperatures than the boundary lines A and D, adjacent to the northern and southern vegetation respectively. At the point level, the pattern was similar with the highest mean radiant temperature values at the central points of square b and c where the granite and stone mosaic paving is not

influenced by any shading or urban geometry, only by direct solar incidence during the whole day. The lowest values of the mean radiant temperature were recorded at the points on the boundaries a and e (at the eastern and western access to the square) due to the influence of shadows generated by the lateral vegetation and by the buildings on the eastern and western sides of the square (which were taller than the buildings on the northern and southern sides). Therefore, the relationship between the width of the public space and the height of the buildings also seems to be a determining factor in the variability of  $T_{MRT}$ . The difference in  $T_{MRT}$  between sunny and shaded areas was found to be less than 3 °C in any time zone.

The proposed methodology to evaluate  $T_{MRT}$  was validated through statistical analysis by comparing the calculated values with simulated values using the urban public comfort simulation software ENVI-met. Results, in Fig. 14, showed a strong coefficient of determination ( $R^2=0.987$ ) comparing all dataset in three time periods. Evaluating the hourly data sets, a valid coefficient of determination of  $R^2=0.8$  and an RMSE of less than 3 % was obtained.

## 11. Conclusion

Urban open spaces provide benefits to citizens as places for outdoor recreation promoting a healthy lifestyle. However, the thermal environment of these spaces is affected by heat stress generated by the urban heat island effect. In order to alleviate the UHI effect, it is important to identify the thermal characteristics of spatial factors of urban areas, and then, promote strategies that improve urban thermal comfort to make public spaces more attractive. For this purpose, it is essential to evaluate thermal radiation, one of the most relevant physical factors of urban thermal comfort. This is summarized in a parameter called mean radiant temperature,  $T_{MRT}$ . To this end, the applicability of two  $T_{MRT}$  measurement methods: thermography and computational simulation, were examined considering the space, materials and design features of an urban square located in the city of Huelva, in Spain.

Airborne thermography was validated as a method after positive results were obtained, achieving high correlations between the in situ measurement and the simulated model (with  $R^2$  values of 0.98 for the whole dataset and 0.8 for each time period data), so this could be extrapolated to another public space in order to evaluate the thermal distribution of  $T_{MRT}$ . However, it should be noted that the presented methodology has some limitations. It is important to mention the variables related to the type of materials covering the urban public space, as well as the percentage of surface area covered by each of them and the vegetation cover. These conditions vary according to the location of the urban space to be analysed within the city and the city itself, depending on its design criteria, the influence of the historical heritage on the choice of pavements and its climate on the choice of vegetation. Regarding methodology, thermography can only assess long-wave thermal radiation, so external data related to solar radiation are needed to evaluate short-wave thermal radiation. In this case, hourly scale data from the nearest weather station was used and a value of short-wave thermal radiation was obtained for each hourly time slot and used to adjust the long-wave mean radiant temperature that was calculated on a point-by-point analysis. The wind data needed for the urban microclimatic simulation was also extracted from the nearest weather station. In future research, only UAVs could be used for the calculation of  $T_{MRT}$  as the versatility of these systems allows the incorporation of multiple sensors on it. Sensors such as pyranometers to measure shortwave radiation in situ, anemometers to measure wind and thermohygrometers to measure air temperature and relative humidity could be installed on the UAV. The ability to fly the UAV at different altitudes and to capture large amounts of terrain in a single flight optimise experimentation time and removes barriers imposed by conventional methods or the use of hand-held thermal cameras from the ground.

For thermal environment evaluation, this kind of research can

support planners and designers working at the macro and micro urban scale. From a general point of view, the point-by-point analysis of thermal distribution as carried out in this research might suggest comfortable routes to create transit-friendly plans, or the identification of weak points with higher thermal radiation to counteract it by using new strategies. For this reason, it is important to explore which factors cause differences in spatial thermal distribution and to propose suggestions for further mitigation.

In this research, the results have shown that  $T_{MRT}$  is influenced by several aspects related to the architectural design of the public space: from the materials covering the square, the existence of vegetation, to urban geometry issues, such as orientation or the height-to-width ratio. In order to assess designers and urban planners in making cities more sustainable, several alternatives are proposed to improve urban thermal comfort such as: the use of cool pavements, the increase of vegetation and green surfaces and the provision of light structures or urban furniture that generate shade and reduce the thermal radiation of the environment.

In relation to material properties, the cool pavements allow counteracting thermal stress in urban public spaces as they have a lower surface temperature. For example, pavements with high solar reflectance are a good choice as they reflect and do not absorb the solar radiation incident on their surface, reaching a lower temperature compared to conventional materials. Vegetation proved to be one of the determining factors in the distribution of  $T_{MRT}$  in this research, as the points with the lowest  $T_{MRT}$  were located next to the palm trees bordering the square. Through reflection and absorption, trees eliminate a large amount of short-wave solar radiation in public spaces. The incorporation of green surfaces and new trees in the centre of the square should result in a lower amount of total radiation. Related to urban geometry, public spaces with high H/W are characterized by less exposure to solar radiation, lower wind speed and lower air temperatures resulting in higher thermal comfort. In large public spaces, such as squares with a low H/W ratio, it is useful to provide light structures or urban furniture that prevent direct solar radiation and generate shade on the pavement.

The main scientific contribution of this work is the validation of aerial thermography as a method to assess the mean radiant temperature, a determining factor of thermal comfort in urban spaces in an automated way, using UAVs that optimize time and economy by reducing the number of operators required. The methodology proposed to achieve it, the results obtained, and the strategies suggested for the improvement of public comfort are expected to be useful to urban designers, construction companies, engineering developers, environmental policymakers and the scientific community in the continued development and expansion of sustainable urbanism.

#### Declaration of Competing Interest

The authors declare that they have no known competing financial interests or personal relationships that could have appeared to influence the work reported in this paper.

#### Data availability

Data will be made available on request.

#### Funding

Funding for open access charge: Universidad de Huelva/CBUA.

Proyecto SALTES (P20\_00730): Smartgrid with reconfigurable Architecture for testing control Techniques and Energy Storage priority. Programa Operativo FEDER 2014-2020 Junta de Andalucía.

#### References

- Niu, J., et al. (2015). A new method to assess spatial variations of outdoor thermal comfort: Onsite monitoring results and implications for precinct planning. *Build. Environ.*, 91, 263–270. <https://doi.org/10.1016/j.buildenv.2015.02.017>
- Kumar, P., & Sharma, A. (2020). Study on importance, procedure, and scope of outdoor thermal comfort –A review. *Sustain. Cities Soc.*, 61. <https://doi.org/10.1016/j.scs.2020.102297>. no. May, p. 102297.
- Rodríguez, M. V., Cordero, A. S., Melgar, S. G., & Andújar Márquez, J. M. (2020). Impact of global warming in subtropical climate buildings: Future trends and mitigation strategies". *Energies*, 13(23), 1–22. <https://doi.org/10.3390/en13236188>
- Lai, D., Liu, W., Gan, T., Liu, K., & Chen, Q. (2019). A review of mitigating strategies to improve the thermal environment and thermal comfort in urban outdoor spaces. *Sci. Total Environ.*, 661, 337–353. <https://doi.org/10.1016/j.scitotenv.2019.01.062>
- Johansson, E., Thorsson, S., Emmanuel, R., & Krüger, E. (2014). Instrumentation and methods in outdoor thermal comfort studies - The need for standardization. *Urban Clim.*, 10(P2), 346–366. <https://doi.org/10.1016/j.uclim.2013.12.002>
- Gómez Melgar, S., Á. Martínez Bohórquez, M., & Andújar Márquez, J. M. (2020). uhuMEBr: Energy Refurbishment of Existing Buildings in Subtropical Climates to Become Minimum Energy Buildings. *Energies*, 13(5), 1204. <https://doi.org/10.3390/en13051204>
- Melgar, S. G., Bohórquez, M.Á. M., & Márquez, J. M. A. (2018). UhuMEB: Design, construction, and management methodology of minimum energy buildings in subtropical climates. *Energies*, 11(10). <https://doi.org/10.3390/en11102745>
- RA-C E. American Society of Heating, ASHRAE Fundamental Handbook 2001. 2001.
- Canan, F., Golasi, I., Ciancio, V., Coppi, M., & Salata, F. (2019). Outdoor thermal comfort conditions during summer in a cold semi-arid climate. A transversal field survey in Central Anatolia (Turkey). *Build. Environ.*, 148, 212–224. <https://doi.org/10.1016/j.buildenv.2018.11.008>
- Lai, D., et al. (2020). A comprehensive review of thermal comfort studies in urban open spaces. *Sci. Total Environ.*, 742. <https://doi.org/10.1016/j.scitotenv.2020.140092>, 140092.
- Fanger, P. O. (1972). *Thermal Comfort: Analysis and Applications in Environmental Engineering*. New York: McGraw-Hill.
- Jendritzky, G., & Nübler, W. (1981). A model analysing the urban thermal environment in physiologically significant terms. *Arch. Meteorol. Geophys. Bioclimatol. Ser. B*, 29 (4), 313–326. <https://doi.org/10.1007/BF02263308>
- Golasi, I., Salata, F., de Lieto Vollaro, E., & Coppi, M. (2018). Complying with the demand of standardization in outdoor thermal comfort: a first approach to the Global Outdoor Comfort Index (GOCI). *Build. Environ.*, 130, 104–119. <https://doi.org/10.1016/j.buildenv.2017.12.021>
- Xi, T., Li, Q., Mochida, A., & Meng, Q. (2007). Study on the outdoor thermal environment and thermal comfort around campus clusters in subtropical urban areas. *Build. Environ.*, 52, 162–170. <https://doi.org/10.1016/j.buildenv.2011.11.006>. July 2012.
- Höppe, P. (1999). The physiological equivalent temperature - a universal index for the biometeorological assessment of the thermal environment. *Int. J. Biometeorol.*, 43(2), 71–75.
- Zhao, X., Luo, Y., & He, J. (2020). Analysis of the thermal environment in pedestrian space using 3D thermal imaging". *Energies*, 13(14). <https://doi.org/10.3390/en13143674>. Jul.
- Naughton, J., & McDonald, W. (2019). Evaluating the variability of urban land surface temperatures using drone observations. *Remote Sens*, 11(14). <https://doi.org/10.3390/rs11141722>
- Song, B., & Park, K. (2020). Verification of accuracy of unmanned aerial vehicle (UAV) land surface temperature images using in-situ data. *Remote Sens*, 12(2). <https://doi.org/10.3390/rs12020288>. Jan.
- H. Guo, D. Aviv, M. Loyola, E. Teitelbaum, N. Houchois, and F. Meggers, "On the understanding of the mean radiant temperature within both the indoor and outdoor environment, a critical review", *Renew. Sustain. Energy Rev.*, vol. 117, no. December 2018, p. 109207, 2020, doi: 10.1016/j.rser.2019.06.014.
- Bedford, T., & Warner, C. G. (1934). The globe thermometer in studies of heating and ventilation. *J. Hyg. (Lond)*, 34(4), 458–473. <https://doi.org/10.1017/S0022172400043242>
- Chen, Y. C., Lin, T. P., & Matzarakis, A. (2014). Comparison of mean radiant temperature from field experiment and modelling: a case study in Freiburg. *Germany*", *Theor. Appl. Climatol.*, 118(3), 535–551. <https://doi.org/10.1007/s00704-013-1081-z>. Nov. VDI. (1994). *VDI 3789, Part 2: Environmental meteorology, interactions between atmosphere and surfaces, calculation of short-wave and long-wave radiation*. Beuth. Berlin.
- Thorsson, S., Lindberg, F., Eliasson, L., & Holmer, B. (2007). Different methods for estimating the mean radiant temperature in an outdoor urban setting. *Int. J. Climatol.*, 27(14), 1983–1993. <https://doi.org/10.1002/joc.1537>. Nov.
- Lee, D. S., Kim, E. J., Cho, Y. H., Kang, J. W., & Jo, J. H. (2019). A field study on application of infrared thermography for estimating mean radiant temperatures in large stadiums. *Energy Build*, 202. <https://doi.org/10.1016/j.enbuild.2019.109360>. Nov.
- Salata, F., Golasi, I., de Lieto Vollaro, R., & de Lieto Vollaro, A. (2016). Urban microclimate and outdoor thermal comfort. A proper procedure to fit ENVI-met simulation outputs to experimental data. *Sustain. Cities Soc.*, 26, 318–343. <https://doi.org/10.1016/j.scs.2016.07.005>. Oct.
- Matzarakis, A., Rutz, F., & Mayer, H. (2007). Modelling radiation fluxes in simple and complex environments - Application of the RayMan model. *Int. J. Biometeorol.*, 51(4), 323–334. <https://doi.org/10.1007/s00484-006-0061-8>
- Lindberg, F., Holmer, B., & Thorsson, S. (2008). SOLWEIG 1.0 - Modelling spatial variations of 3D radiant fluxes and mean radiant temperature in complex urban settings. *Int. J. Biometeorol.*, 52(7), 697–713. <https://doi.org/10.1007/s00484-008-0162-7>

- Du, J., Sun, C., Liu, L., Chen, X., & Liu, J. (2021). Comparison and modification of measurement and simulation techniques for estimating Tmrt in summer and winter in a severely cold region. *Build. Environ.*, 199. <https://doi.org/10.1016/j.buildenv.2021.107918>
- Cohen, S., et al. (2020). Mean radiant temperature in urban canyons from solar calculations, climate and surface properties – Theory, validation and ‘Mr.T’ software. *Build. Environ.*, 178. <https://doi.org/10.1016/j.buildenv.2020.106927>. Jul.
- J. Acuña Paz y Miño, C. Lawrence, and B. Beckers, “4π Thermograms : A ProjectionTo Understand Thermal Balance”, in Proceedings of Building Simulation 2019: 16th Conference of IBPSA, Mar. 2020, vol. 16, pp. 448–455, doi: 10.26868/25222708.2019.210969.
- Videras Rodríguez, M., Melgar, S. G., Cordero, A. S., & Márquez, J. M. A. (2021). A Critical Review of Unmanned Aerial Vehicles (UAVs) Use in Architecture and Urbanism: Scientometric and Bibliometric Analysis. *Appl. Sci.*, 11(21), 9966. <https://doi.org/10.3390/app11219966>. Oct.
- Gaitani, N., Burud, I., Thiis, T., & Santamouris, M. (2017). High-resolution spectral mapping of urban thermal properties with Unmanned Aerial Vehicles. *Build. Environ.*, 121, 215–224. <https://doi.org/10.1016/j.buildenv.2017.05.027>
- Feng, L., Tian, H., Qiao, Z., Zhao, M., & Liu, Y. (2020). Detailed Variations in Urban Surface Temperatures Exploration Based on Unmanned Aerial Vehicle Thermography. *IEEE J. Sel. Top. Appl. Earth Obs. Remote Sens.*, 13, 204–216. <https://doi.org/10.1109/JSTARS.2019.2954852>
- Park, K., Christensen, K., & Lee, D. (2020). Unmanned aerial vehicles (UAVs) in behavior mapping: A case study of neighborhood parks. *Urban For. Urban Green*, 52. <https://doi.org/10.1016/j.ufug.2020.126693>. April, p. 126693.
- Peel, M. C., Finlayson, B. L., & McMahon, T. A. (2007). Updated world map of the Köppen-Geiger climate classification. *Hydrol. Earth Syst. Sci.* <https://doi.org/10.5194/hess-11-1633-2007>
- Annual climatological values. Huelva, Ronda Este - Agencia Estatal de Meteorología (AEMET). Gobierno de España. <http://www.aemet.es/es/serviciosclimaticos/datosclimatologicos/valoresclimatologicos?l=4642E&k=and> (accessed Feb. 16, 2022).
- Meteorological values for the last 24 hours - Weather Station Huelva, Ronda Este. <https://x-y.es/aemet/est-4642E-huelva-ronda-este> (accessed Feb. 18, 2022).
- Calculation of the position of the sun in the sky for every location at any time. [https://www.sunearthtools.com/dp/tools/pos\\_sun.php](https://www.sunearthtools.com/dp/tools/pos_sun.php) (accessed Feb. 18, 2022).
- Solar Radiation - Agencia Andaluza de la Energía. Junta de Andalucía. <http://www.agenciaandaluzadelaenergia.es/Radiacion/radiacion1.php> (accessed Feb. 18, 2022).
- New Regulatory framework on UAV/UAS/Drones - Agencia Estatal de Seguridad Aérea (AESA). Gobierno de España. [www.seguridadaerea.gob.es](http://www.seguridadaerea.gob.es) (accessed Feb. 18, 2022).
- Kántor, N., & Unger, J. (2011). The most problematic variable in the course of human-biometeorological comfort assessment - The mean radiant temperature”, *Cent. Eur. J. Geosci.*, 3(1), 90–100. <https://doi.org/10.2478/s13533-011-0010-x>
- E.A. Arens et al., “ANSI/ASHRAE Addendum g to ANSI/ASHRAE Standard 55-2013 Thermal Environmental Conditions for Human Occupancy”, vol. 8400, 2016.
- Höppe, P. (1992). Ein neues Verfahren zur Bestimmung der mittleren Strahlungstemperatur in Freien. [A new measurement procedure to obtain the mean radiant temperature outdoors]. *Wetter und Leb*, 44, 147–151.
- VDI VDI 3787, Part 1: Environmental Meteorology.methods for the human-biometeorological evaluation of climate and air quality for the urban and regional planning at regional level, Beuth. Berlin, 1998.
- VDI VDI 3789, Part 3: Environmental Meteorology, interactions between atmosphere and surfaces; calculation of spectral irradiances in the solar wavelength range, Beuth., vol. Beuth, Ber. Berlin, 2001.
- Campbell, G. S., & Norman, J. M. (1998). *An Introduction to Environmental Biophysics*. Springer New York.
- Tsoka, S., Tsikaloudaki, A., & Theodosiou, T. (2018). Analyzing the ENVI-met microclimate model’s performance and assessing cool materials and urban vegetation applications—A review. *Sustain. Cities Soc.*, 43, 55–76. <https://doi.org/10.1016/j.scs.2018.08.009>
- Fabbri, K., & Costanzo, V. (2020). Drone-assisted infrared thermography for calibration of outdoor microclimate simulation models. *Sustain. Cities Soc.*, 52. <https://doi.org/10.1016/j.scs.2019.101855>. Jan.
- Du, J., Sun, C., Liu, L., Chen, X., & Liu, J. (2021). Comparison and modification of measurement and simulation techniques for estimating Tmrt in summer and winter in a severely cold region. *Build. Environ.*, 199(66). <https://doi.org/10.1016/j.buildenv.2021.107918>. p. 107918.
- Naboni, E., Meloni, M., Coccolo, S., Kaempff, J., & Scartezzini, J. L. (2017). An overview of simulation tools for predicting the mean radiant temperature in an outdoor space. *Energy Procedia*, 122, 1111–1116. <https://doi.org/10.1016/j.egypro.2017.07.471>
- Gál, C. V., & Kántor, N. (2020). Modeling mean radiant temperature in outdoor spaces, A comparative numerical simulation and validation study. *Urban Clim*, 32, Article 100571. <https://doi.org/10.1016/j.uclim.2019.100571>. April 2019.
- A. Claudia Carfan, E. Galvani, and J. Teixeira Nery, “Study of thermal comfort in the City of São Paulo using ENVI-met model, 2020.
- Willmott, C. J. (1981). On the validation of models. *Phys. Geogr.*, 2(2), 184–194. <https://doi.org/10.1080/02723646.1981.10642213>